**Title:** Influence of dry and wet seasons on pore distributions of near-surface weathered granitic soil using mercury intrusion porosimetry and nuclear magnetic resonance imaging

**Authors:** Ran AN [1,2*], Yixian WANG[1,*], Xianwei ZHANG[2], Cai Sutong[3], Chen Chang[3]

**All Author's Institution**:

1. School of Civil and Hydraulic Engineering, Hefei University of Technology, Hefei 230009, China;

2. State Key Laboratory of Geomechanics and Geotechnical Engineering, Institute of Rock and Soil Mechanics, Chinese Academy of Sciences, Wuhan, China;

3. College of Urban Construction, Wuhan University of Science and Technology, Wuhan 430065, China.

**Author 1 ( *Corresponding Author )**: Ran An, Associate Professor, E-mail: anran@wust.edu.cn; ORCID: https://orcid.org/0000-0003-2388-3160.

**Author 2:** Yixian Wang, Professor, E-mail: wangyixian2012@hfut.edu.cn

**Author 3:** Xianwei Zhang, Professor, E-mail: xwzhang@whrsm.ac.cn

**Author 4:** Sutong Cai, Ph.D candidate, E-mail: caisutongqq@163.com

**Author 5**: Chang Chen, Master candidate, E-mail: changchen99@outlook.com

**Key Points:**

Micro-pores in granite residual soil gradually expand and connect with macro-pores due to wetting-drying cycles

The deterioration of the granite residual soil structure was observed based on $T_2$-weighted images

The method of estimating soil porosity using NMR data is proved to be feasible and accurate

**Abstract:** The near-surface weathered granitic soil (WGS) is easily affected by cyclic drying and wetting due to seasonal alterations. The microstructural damage was characterized using the technology of nuclear magnetic resonance (NMR) imaging and mercury intrusion porosimetry (MIP) to study the influence of dry and wet seasons impacts on microstructures of soils. The results revealed that the relaxation time (T2) spectrums from NMR investigation were strongly affected by multiple wetting-drying cycles, and the porosity had a positive nonlinear relationship with the peak areas. As implied in the MIP and NMR analysis, PSD curves of WGS were characterized by bimodal distributions as the pore diameter in two peaks ranging from 0.1 μm to 5 μm and 5 μm ~100 μm, respectively. As the number of cycles increases, the left peak of the PSD curve successively shifts downwards while the right peak shifts upwards, implying that a large number of small-sized micro-pores in the WGS gradually expand and connect to macro-pores. Under the influence of periodic water migrations in soils, the areas of bright spots in the $T_2$-weighted images increased, reflecting that the structural damage degree was accelerated with continued enlargement of internal pores. Through a comparison between NMR-based and MIP-based PSDs, NMR can better capture more accurate information on the pore distribution attributed to its advantage of test principle and nondestructive scanning. The process of cyclic wetting and drying severely reformed the microstructure of the WGS, causing the micropores to gradually expand to form macropores and thus deteriorating the soil microstructure.

**Keyword:** weathered granitic soil, wetting-drying cycles, nuclear magnetic resonance imaging, mercury intrusion porosimetry, pore distributions

## 1 Introduction

Soil microstructure, which is closely associated with engineering properties, refers to the size, shape, and arrangement of solid particles and pores in soil and the contacting forms and connections between them (Burton et al., 2014, Baer et al., 2009). The deformation and strength characteristics of soil can be considered a comprehensive effect of the adjustment and evolution of its microstructural feature (Tuller and Or 2001, An et al., 2023). The pore size distribution (PSD), as a vital intrinsic factor of soils, significantly influences the physical, hydraulic, and mechanical behaviors of soils, such as permeability, soil-water characteristic curves, and shear strength(Duan et al., 2018, Ying et al., 2021, Zhang et al. 2023). The pore structure in the soil is a dynamic system influenced by external changes resulting from natural or artificial factors(Vogel et al., 2005., Pires et al., 2008). The action of wetting-drying cycles is regarded as a crucial effect applied to the soil microstructure, peculiarly in hot and rainy climate (Zhao et al., 2017, Tang et al., 2020, An et al., 2022a). Laboratory and in-situ investigations have concluded that wetting-drying cycles cause remarkable changes for the physical and mechanical properties of soils deperived from granite (Ng et al., 2009, Burton et al., 2015, Liu et al., 2020). Several studies have reported that the wetting-drying cycles caused a critical modification of the soil microstructure (Pires et al., 2020, Huang et al. 2021).

Soils derived from weathering granite are widely distributed in tropical and subtropical regions, where the drying and wetting season provides a condition of the physical and chemical weathering for rocks (Blight and Leong, 2012, Liu et al., 2022). The near-surface weathered granitic soil (WGS) is characterized by high voids ratio, considerable shrinkage deformation, and multiple fissures, owing to a reduction in moisture content (Da et al., 1997, Coutinho et al., 2019). Under weathering and deposition effects, the microstructure in WGS is highly determined by climatic variations (Otalvaro et al., 2015). Furthermore, the soils deprived from granite may collapse ascribed to the coupling action of external loading and wetting (Rao and Revanasiddappa 2006). The near-surface WGS is prone to be disintegrated into smaller soil blocks under the condition of water immersion (Liu et al., 2021). The water sensitivity of soils has played an essential role in the sinking of boreholes for piling. For instance, excavation for grout piles is a common foundation method used in these soils in southern China (Luan et al., 2018). During heavy rain, the soil within the sidewalls of the drilled boreholes is saturated rapidly with rainfall infiltration (Kusuma and Leong 2014, Meng et al., 2020). The boreholes are particularly vulnerable to collapse, though some protection measures such as water pumping are

74 applied. Consequently, the bearing capacity and modulus of deformation of piles fall below their
75 designed values in engineering practice. During rainy seasons, near-surface soils, which are deprived
76 from granite, contain a large proportion of clay minerals and fissures. Due to the loss of suction, they
77 wet faster, lose more strength, and form landslides or debris flows compared to more plastic soils
78 (Okewale and Coop 2018, Ng, et al., 2019).
79 In recent years, a series of studies have been conducted to assess the effects of wetting-drying cycles on
80 the structural change of soils deprived from granite. Kong et al. (2018) suggested that the soil-water
81 characteristic curve of residual soil considerably changes with the increasing number of wetting-drying
82 cycles and that pore expansion is the major reason for this phenomenon. An et al. (2022a) verified that
83 the effect of wetting-drying cycles has a multi-scale influence on natural WGS, especially in shear
84 strength, particle connections, soil fabric, and cracking behavior. Sun et al. (2022) performed a set of
85 tests to reveal the microstructural properties, such as microtopography and chemical composition, to
86 demonstrate the evolutionary mechanism of the disintegration properties of WGS. These studies have
87 validated that the soil microstructure is of great significance for engineering accidents of WGS because
88 of climatic alternations. Nonetheless, there are few investigations on the pore size distribution of WGS
89 under the effects of cyclic wetting and drying.
90 Various testing methods have been applied to analyze the pore size distributions, such as scanning
91 electron microscope (SEM), X-ray computed tomography (CT), mercury injection porosimeter (MIP),
92 and nuclear magnetic resonance (NMR) scanning (Suzuki 2002, Suits et al., 2002, Starnon et al. 2017,
93 Zhang et al., 2017, Kong et al., 2018). MIP technology is common effective means to measure the pore
94 distribution of soil in geotechnical investigations (Watanabe and Osada 2016). MIP with a simple
95 process, rapid measurement, and a wide range of pore sizes is generally regarded as one of the
96 suggested methods for measuring pore volumes in geomaterials. The measurement of MIP is based on
97 the capillary phenomenon, in which non-wetting liquids incrementally enter the porous space at
98 different mercury pressure. It is assumed that the pores in soils are capillary bundles with different
99 apertures and mercury volume entering the samples is correlated with a function of external pressure
100 (Jian et al., 2015). Therefore, the pore size distribution can be obtained by measuring the volume of
101 mercury. It has been confirmed that MIP has good applicability in measuring the distributions of pore
102 diameters, while its authenticity remains unclear (Robin et al., 2016, He et al., 2018). The nuclear
103 magnetic resonance (NMR) technique is an effective method for non-destructive detection of the pore

104 distribution of soil regarding quantitative and visual forms (Tian et al. 2019). Through the measurement
105 of NMR relaxation time ($T_2$) spectrums, the hydrogen nuclei in bound water, capillary water, and free
106 water can be detected at a nano-sized accuracy (Webber et al. 2013). Besides, the imaging function
107 attached to an NMR instrument provides an effective method to qualitatively identify the spatial
108 distribution of pore water in the specimen (An et al. 2022b). With its development and application,
109 NMR imaging has become a vital technique and is broadly employed to explore the pore structure of
110 rocks and soils due to several advantages, such as non-destructive, precise, and quantitative detection
111 (Yao et al., 2012). Since the $T_2$ spectrums of targeted molecules reflect the structural arrangements of
112 surrounding water molecules, the NMR may shed insights into the pore size distribution and moisture
113 migrations in soils under dry and wet seasons(Yu et al., 2019). However, the application of NMR to
114 investigate the environmental effect on soil microstructure has not been validated. Hence, it is of great
115 significance to research the pore size distributions of WGS by combining MIP and NMR techniques.
116 The presented manuscript aimed to characterize the pore size distribution of the near-surface WGS and
117 the influence of wetting-drying cycles on soil microstructure. A set of NMR and MIP analyses was
118 performed on undisturbed samples to demonstrate environmental effects from both quantitative and
119 visual perspectives. The results facilitate the cognition of the microcosmic mechanism of
120 environmental damage on soils subject to geothermal circumstances.

121 **2 Materials**

122 2.1 Engineering background

123 As shown in Figure. 1a, the sampling site was located in Shenzhen, Guangdong in China (longitude
124 114°04' E, latitude 22°46'N). The climate of Shenzhen is characterized by a high annual temperature
125 (23.3℃) and a rich annual precipitation (1932.5 mm). Besides, it has distinct rainy and dry seasons.
126 According to geological survey, the major geologic bodies encountered in metro tunnel sections in
127 Shenzhen is the WGS and highly-weathered granite. The geological profiles of the sampling site is
128 presented in Fig. 1b. The soil layers within the tunneling ranges were divided into the five types
129 including NS-1 (planting soil at depth of 0 - 1.2 m), NS-2 (subgrade filling with stones at depth of 1.2 –
130 2.8 m), NS-3 (reddish brown sandy clay at depth of 2.8 m - 9.4 m), NS-4 (yellowish brown
131 sandy/gravel clay at depth of 9.4 m - 18.8 m), and NS-5 (strongly weathered granite at depth of 18.8 m
132 - 22.5 m).

The drilling technique was used for sampling the soils at depths of 3.5 – 9.5 m from an open-cut slope, which experienced the alternation of arid and rainy seasons for a long term. Undisturbed samples with nature mositure contents were then properly preserved and transported to the laboratory. The soil samples used in this study is collected at the layer of NS-3 and typically classified as sandy clay via geotechnical investigations. Due to the groundwater level of this sampling site is about 3.8 m, the studied soil is collected at the near-surface layers which exposed atmospherically and thus frequently affected by rainfall infiltration and evaporation.

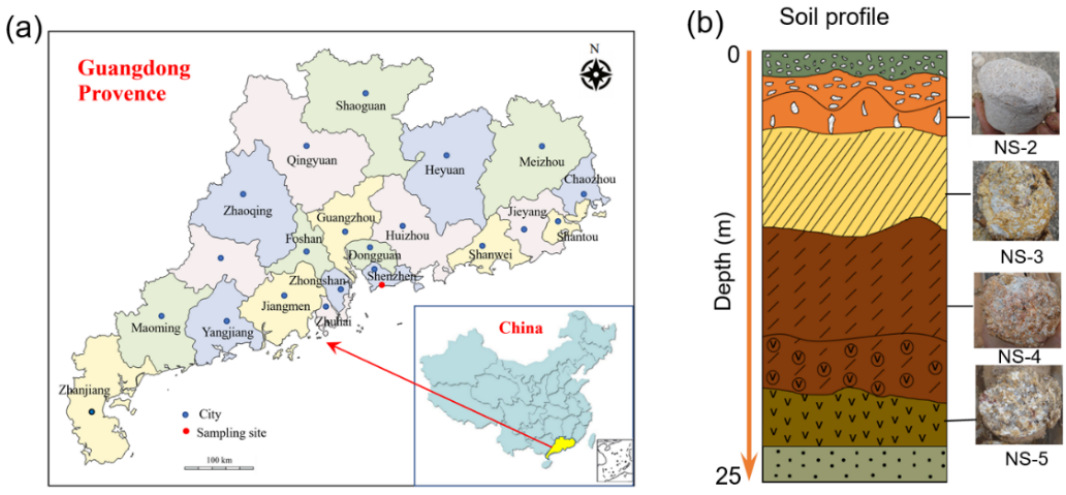


Figure. 1 Profile of the sampling site: (a) geographical location; (b) geological sections.

## 2.2 Soil properties

The fundamental physical properties of the natural soil were determined the ASTM standards (D2166-16 [2016], D5084–16 [2017], D4767–11 [2020]). A summary of these paramenters is listed in Table 1. Also, the mineral compositions were tested according to result of XRD diffraction pattern. The WGS is mainly composed of clay minerals including kaolinite (41.4%) and small amount of illite (5.6%), as well as non-clay minerals including quartz (50.7%) and hematite (2.3%). Concerning grading characterization of soils, particle sizes greater than 0.075 μm were determined by sieving, and the finer fractions were tested by the hydrometer test according to ASTM D7928 (2017). The ternary phase diagram of grain compositions (Fig. 3) classified the WGS that contains high contents of clay and sand grains into sandy clay, which is similair to the classification result proposed by Zhang et al. (2022).

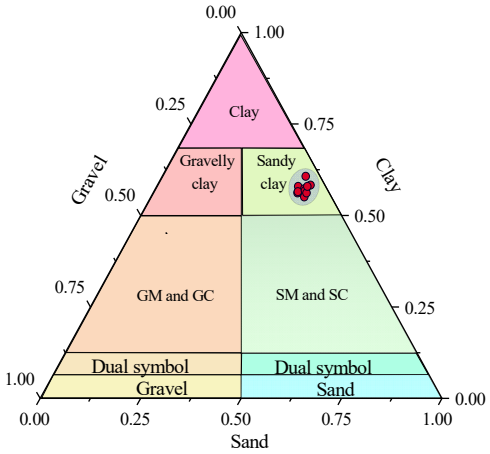


Figure. 2 The grain-size distributions of WGS

**Table 1** Physical and mineralogical properties of the WGS.

| Index | Average value |
|---|---|
| Moisture content, $w_n$ (%) | 26.8 |
| Bulk density, $\rho_b$ (g/cm$^3$) | 1.76 |
| Void ratio, $e$ (%) | 0.68 |
| Liquid limit, $w_L$ (%) | 56.4 |
| Plasticity limit, $w_P$ (%) | 24.3 |
| Plasticity index, $I_P$ | 32.1 |
| Hydraulic conductivity, $K$ (cm/s) | $8.5\times10^{-6}$ |
| Unconfined compressive strength (kPa) | 178.6 |
| Effective Cohesion, $c'$ (kPa) | 47.5 |
| Effective internal friction angle, $\varphi'$ (°) | 24.8 |

## 3 Experiment procedure

### 3.1 Peocedure of wetting-drying cycles

As shown in Fig. 4, a complete procedure of cyclic drying and wetting treatments begins at the lowest mositure content $w_{min}$ under drying treatment, then underwent a wetting procdure to reach saturated mositure content $w_{sat}$ and ends at the $w_{min}$ after drying. For each drying procedure, the specimen was dried in for 12 hours in an incubator with the temperature 40°C and relative humidity of 50% to reach the $w_{min.}$ For each wetting procedure, the specimen was vacuumized and saturated by distilled water to

its $w_{sat}$ and then immersed for 24 hours to ensure fully saturated. The relaxation time ($T_2$) spectrums and NMR images were captured once the specimen was humidified to the $w_{sat}$ for obtaining pore distribution under different number of wetting-drying cycles.

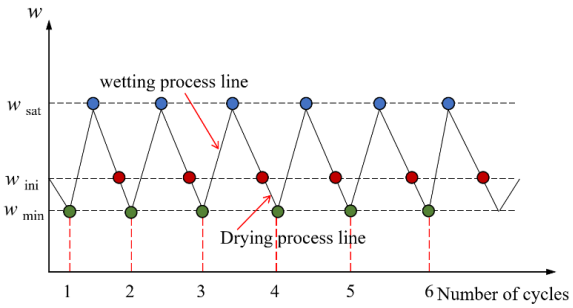


Fig. 3 Flowing diagram of wetting-drying cycles.

**3.2 Testing methods**

3.2.1 Measurement of nuclear magnetic resonance imaging

The tests of NMR imaging were performed on an AniMR-150 NMR imaging system, which is produced by Suzhou Niumag Analytical Instrument Co., Jiangsu, China. The permanent magnet of this instrument is 0.5 T and the corresponding proton resonance frequency is 25.76 MHz at 25°C. The transverse relaxation time ($T_2$) and NMR images were obtained by using NMR technology. The specific experimental procedure is demonstrated in Fig. 4. Before experiments, a cylinder specimen with a size of 38 mm in diameter and 80 mm in height was firstly dried up to its moisture content reached 12% and then vacuum saturated to perform the drying and wetting treatment. Afterwards, the NMR imaging procedure was initiated to accurately measure the $T_2$ spectrums and $T_2$-weighted pseudo-color images of the near-surface WGS.

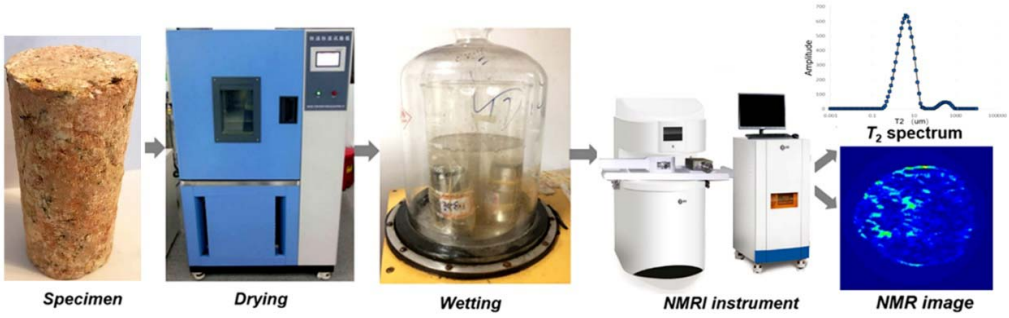


Fig. 4 The diagram of the major experiment procedure.

3.2.2 Measurement of mercury intrusion penetration tests

The changes in the pore size distribution (PSD) induced by wetting-drying cycles were investigated

through the MIP measurements using a Pore Master-33 mercury injection instrument produced by Quantachrome Instruments Company. This instrument can identify the pores with sizes ranging from 0.01 um to 300 um. Before the tets, soil specimens were trimmed into cubic solid smaller than 1.0 $cm^3$ from the undisturbed sample. Then, the specimens were rapidly immersed in liquid nitrogen and freezed at −56 °C for 2 days so that they were water-free. Ultimatly, the mercury is gradually injected into soil by incresing the mercury intrusion pressure. According to a classical formula proposed by Washburn (1921), the relationship between mercury pressure $p$ and the pore size $D$ is provided as the following formula:

$$p = \frac{-4\sigma_{hg}\cos\theta_{ms}}{D} \quad (1)$$

Where, $\sigma_{hg}$ is the mercury surface tension, which is 0.484 N/m. $\theta$m is the contacting angle of soil particles and mercury, which is 140°.

3.2.3 Scanning electron microscope

To investigate the varaition of the soil microstructure under wetting and drying cycles, tests of scanning electron microscope (SEM) were performed on the specimens at different number of wetting-drying cycles. The microstructural morphology in the small-sized specimen with with 10 mm side-length was captured and qualitatively observed using a Quanta-250 SEM instrement.

## 4 Theoretical backgrounds of NMR and PSD analysis

The basic principle of NMR imaging analysis is that a system of spin nuclei in a magnetic field absorbs externally matched radio frequency (RF) energy, which is the same as that of the spin nuclear system (Yao and Liu 2012). The signal amplitude indicates the present protons in pore water, and the relaxation time ($T_2$) denotes the rate at which the precession of hydrogen nuclei gradually decays in an inhomogeneous magnetic field. Additionally, the $T_2$-weighted images of the specimen were obtained by spin-echo (SE) sequences with the $T_2$ echo time (TE) of 60 ms and $T_2$ repetition time (TR) of 1800 ms. Accordingly, the NMR technology is sensitive to hydrogen fluids in porous media and is a non-invasive method for characterizing the pore water distribution in soils (Stingaciu et al., 2009).

The $T_2$ value is determined by pore sizes, fluid properties, and testing parameters, as well as the magnetic field properties. However, diffusion relaxation can be ignored in a low, uniform magnetic field. Moreover, bulk relaxation can also be neglected because it takes much longer time than surface

relaxation for water in nonmagnetic materials. Thus, the $T_2$ can be simply measured as:

$$\frac{1}{T_2}=F_s\frac{\rho_2}{r} \quad (2)$$

where $\rho_2$ denotes the coefficient of surface relaxivity, which is related to the specific mineral grains for a particular soil; $r$ represents the equivalent pore diameter; $F_s$ indicates the shape parameter, which is widely verified to be 4 for pores in soils by previous researchers (Kong et al. 2018, Ma et al. 2021)..

As revealed in Eq. (2), the value of $\rho_2$ is an essential parameter to characterize the pore size. Although the $\rho_2$ varies with the mineralogical composition of the soil, it is a constant for a specific soil and is independent from temperatures and pressures. Several methods were proposed to estimate the $\rho_2$ values of pore solid medium. The value of $\rho_2$ can be calculated by applying the PSD data by performing MIP measurements(Kenyon 1992; Yao and Liu 2012).

## 5 Results and discussions

### 5.1 MIP results

The changes in PSD of the near-surface WGS under different numbers of wetting and drying cycles were obtained by MIP measurements, as illustrated in Fig. 5. The PSD curve providing the relationship between incremental intrusion volumes and pore diameters of the natural specimen ($N$=0) exhibited a bimodal distribution with a high peak ranging from 0.1 to 5 μm and a low one ranging from 5 to 100 μm in pore diameter. The pore volumes with a diameter smaller than 1 um decreased due to wetting-drying cycles, while the pore volumes with a diameter larger than 10 um in PSD curves significantly increased, reflecting the initiation and progression of interconnected cracks. As $N$ increased from 1 to 5, the PSD curve shifted rightward, and the volume of accumulative intrusion enlarged.

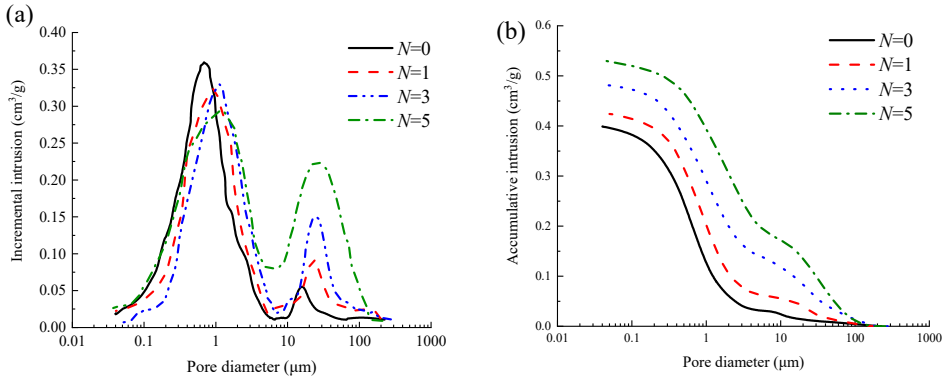

**Fig. 5** Results of MIP measurements

### 5.2 $T_2$ spectrums and total porosity

The transverse relaxation time $T_2$ is associated with the size of pores in soils, and the value of $T_2$ is proportional to the volume of pores. Thus, the change of $T_2$ values and signal spectrum integral area can reflect the variations of total pore volume in soils. In this section, the distribution curves of transverse relaxation times $T_2$ were analyzed, and the peak positions and areas of each peak were calculated. The $T_2$ relaxation spectrum curves presenting a bimodal distribution of the WGS are depicted in Fig. 6. The dominant peak is to the left of the abscissa, and its $T_2$ distribution range from 0.6 to 25 ms. The minor peak is to the right of the abscissa, and its $T_2$ value ranges from 5 to 50 ms. With the increasing number of cycles, the maximum value of the dominant peaks slightly declines, while that of minor peaks sharply increases. After the 8th cycle, the maximum value of the dominant peak and minor peak decreased by 7.54% and 417.13%, respectively.

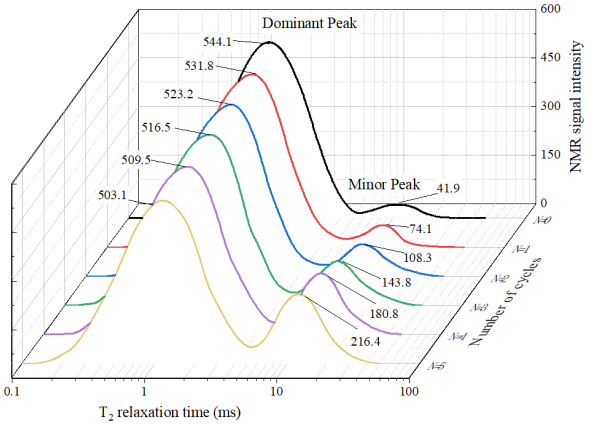


**Fig. 6** $T_2$ distribution curves with the number of wetting-drying cycles

In NMR experiments, the relaxation time $T_2$ of the specimen at a fully-saturated state demonstrates the quantitative information of pore size. The $T_2$ value is supposed to be positively correlated with the equivalent pore diameter. Furthermore, the total area of peaks in the $T_2$ spectrums is positively related to the porosity (Kenyon 1992). In this study, the total area of peaks of each $T_2$ spectrum was calculated, and a linear relationship with the volume of accumulative intrusion was established, as illustrated in Fig. 7. Data fitting revealed that the volume of accumulative intrusion increased linearly with the increase in a total area of peaks. The linear equation presented in Fig. 7 achieved a good result as the square of their correlation coefficients reached 0.99, verifying the feasibility and accuracy of using NMR data to estimate the soil porosity.

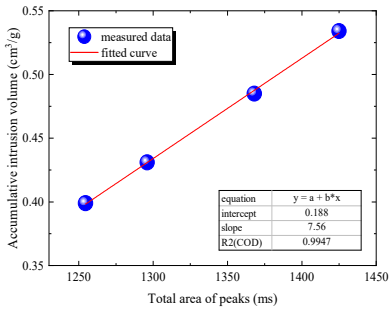


**Fig. 7** The relationship between total porosity and peak area

### 5.3 NMR-based pore size distributions

The value of $\rho_2$ of the studied soil is derived by using Kenyon's principle, and the value is 0.463 μm/ms. Hence, $r$ can be calculated from the $T_2$ values following Eq. (2). The probability distributions of pore volume with different sizes and the accumulative porosity were obtained by the $T_2$ spectrum from NMR measurements. The probability distribution curves of the soil sample with different wetting-drying cycles maintained bimodal distributions, as displayed in Fig. 7. According to the data of $T_2$-based pore size distribution curves, the pores in WGS under different wetting and drying cycles were classified into micropores and macropores upon their diameters. The peak indicating micro-pores was distributed between 0.05 and 5 μm, and the peak representing macro-pores was distributed between 5 and 100 μm. Additionally, the comparison of the probability curves of pore size distribution suggested that the proportion of the micro pore and macro pore decreased and increased with increasing wetting-drying cycles, respectively. The distribution histogram of the pore diameters is exhibited in Fig. 8. The distribution of pore size in WGS had a significant variation by the influence of multiple wetting-drying cycles. The most prominent changes were the decrease in the proportion of pores with a diameter range of 0.01 to 5 μm, whereas the proportion of pores with a diameter of more than 5 μm increased. After the 8th cycle, the proportion of pore diameter below 5 μm decreased from 91.15% to 56.04%, and the proportion of pore diameter between 5 and 100 μm increased from 9.85% to 43.96%. This phenomenon implied that a large number of micro-pores with small sizes in WGS gradually expanded and connected into macro-pores during the process of wetting-drying cycles.

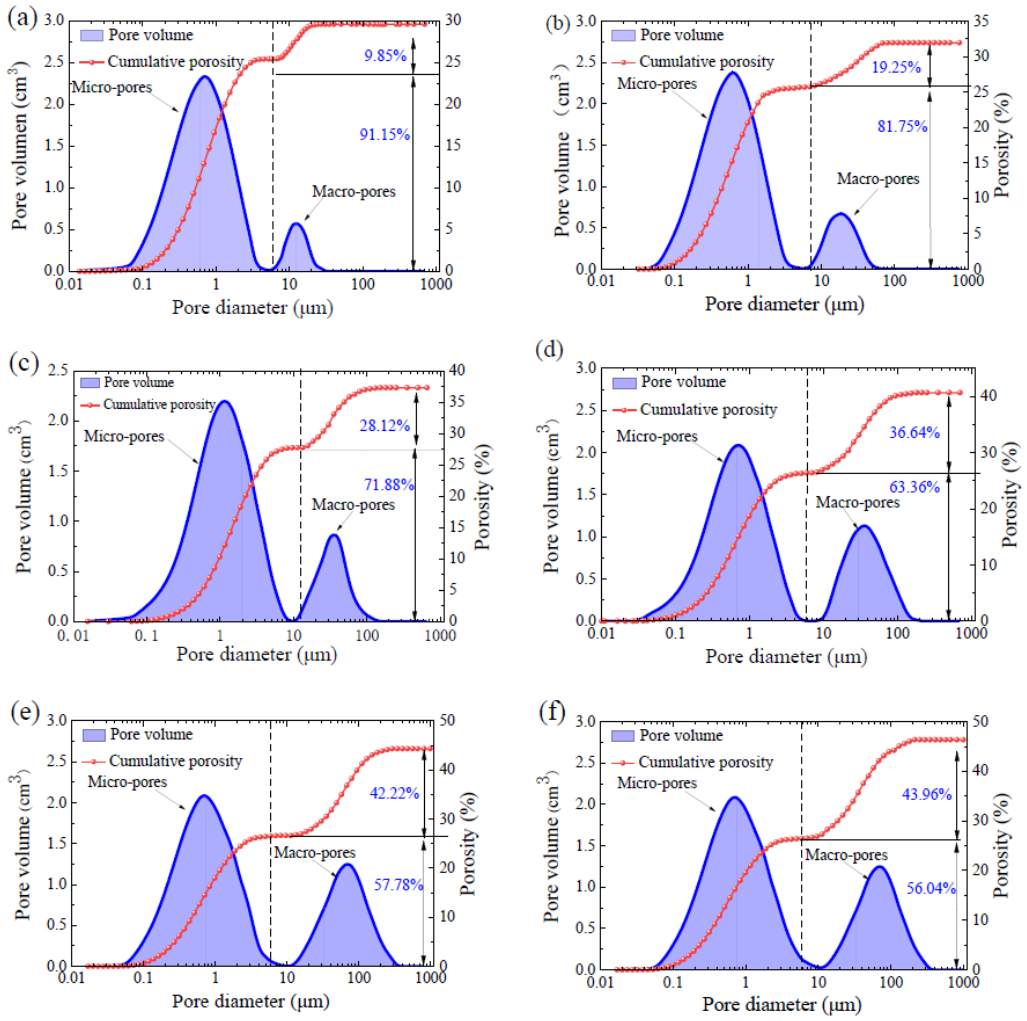


**Fig. 8** The curves of pore size distribution.

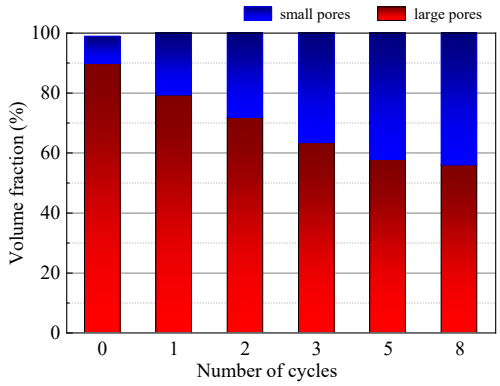


**Fig. 9** The volume fractions of pores with different sizes.

### 5.4 $T_2$ weighted images from NMR tests

Fig. 10 exhibits the pseudo-color NMR images ($T_2$ weighted images), in which the color bars denote

the relative signal intensity of the fluid in the pore containing hydrogen nuclei of the soil specimens under different wetting-drying cycles. In the NMR image, dark blue areas indicate that hydrogen atoms are not contained in the sample, namely, no imaging signal; red areas suggest water in the pores, and thus the high proton density demonstrates a strong NMR signal. The $T_2$ weighted images of both transverse and vertical cross-sections from NMR imaging were captured to visualize the changing patterns of pore structures. The distribution of pores could be visually discerned according to the feature of the $T_2$ weighted images in Fig. 10. As observed in Fig 10 (a), the $T_2$-weighted image of the initial specimen is comparatively homogeneous with few light spots in soil, reflecting that the original voids are mostly micro-pores. Fig. 10 (b) illustrates a few bright spots at the central portion of the images after the first cycle of wetting-drying, demonstrating that the macro-pores in soil appear to initiate and develop. As revealed in Figs. 10 (c)-(f), the phenomenon of expanding luminous spots in $T_2$-weighted images is significant. In other words, more micro-pores have gradually connected into macro-pores. The NMR imaging results unveiled that the areas of light spots increased, as well as their luminance, implying an increasing volume of pores. The enlargement in the luminous area and inhomogeneity of NMR images with the increasing number of wetting-drying cycles is associated with the continued development of microstructural damage. Accordingly, the results from NMR imaging visually illuminated the expansion of pore contents and the deteriorated degree of soil microstructure under the influence of alterations of dry and wet seasons.

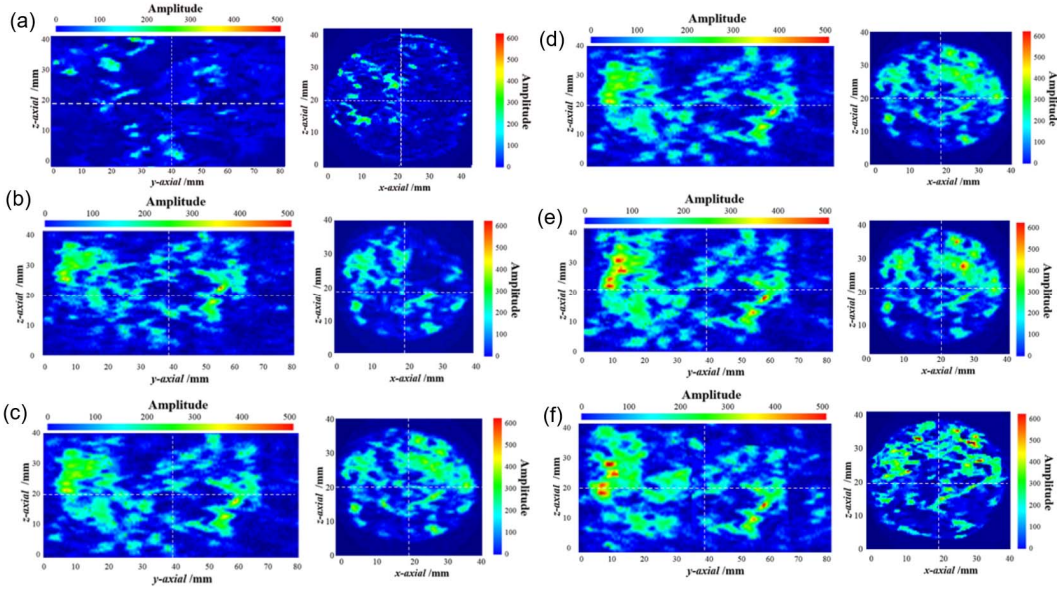

**Fig. 10** $T_2$-weighted images of the specimen under different number of wetting-drying cycles: (a) $N$=0; (b) $N$=1; (c) $N$=2; (d) $N$=3; (e) $N$=5; (f) $N$=8.

## 6. Discussions

### 6.1 Comparison between MIP and NMR

The technology of NMR imaging and MIP was applied to study the influence of dry and wet seasons impacts on microstructures of WGS. From Fig. 11(a) to (d), there are some similarities and discrepancies between the curves of pore volume distribution from NMR and MIP. It can be observed that the shape of bimodal distributions of WGS is well consistent. Moreover, the most probable values of pore diameters from NMR and MIP are close to each other. Therefore, the NMR measurements can be viewed as efficient tools for qualifying the distributions of pore size in soils. Theoretically, both MIP and NMR reflect the pore structures in porous mediums. Thus, the pore size distributions from these two methods keep completely consistent in idealized conditions (Ohkub et al., 2016). Nevertheless, the pore volume distributions obtained by the two methods have significant differences, especially in the micro-pores of right peaks. Compared to the NMR results, the volume of macro-pores is underestimated, while the proportion of micro-pores is relatively overestimated from the MIP measurements in this study. This is in that the method for obtaining pore size distribution by MIP and NMR has a difference in their physical principles. Concerning NMR technique, the total volume of hydrogen in pore water can be accurately detected for a fully saturated specimen, allowing the measurements of pore volume from NMR to infinitely approach the true values. With respect to the MIP technique, the pores in tested specimens to the maximum mercury inlet pressure can only be measured by mercury injection. Considering that the morphology and connectivity of pores in soils are complicated, it is difficult for the mercury saturation of macro-pores to reach 100% (Tian and Wei 2020). The requirement of testing conditions during MIP tests should be carefully adjusted to realize a more accurate mercury injection. However, high injecting pressures may either deform or damage the original pore structure with large sizes and induce suspect results. As a result, the measurements of MIP are less accurate than that of NMR, which is completely non-destructive and has high accuracy.

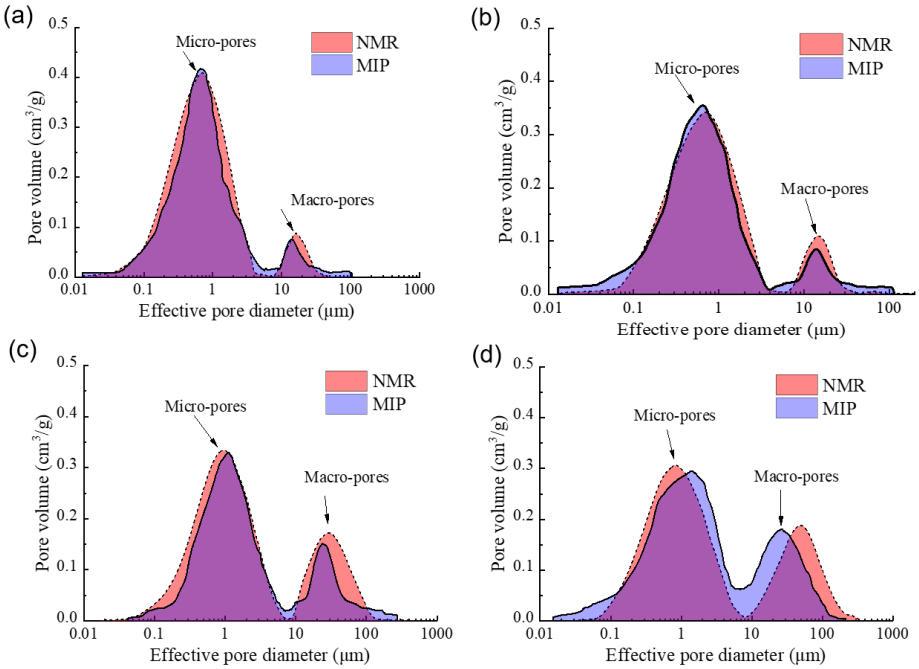


**Figure 11.** Pore volume distributions from NMR and MIP results under different number of wetting-drying cycles: (a) *N*=0; (b) *N*=1; (c) *N*=3; (d) *N*=5.

### 6.2 Microscopic mechanism analysis

There are a large amount of clay and sand grains in sand, enabling the grain size distribution to exhibit a bipolarized distribution. Under the natural environment of dry and wet seasons, the sand grains with quartz as the main crystalline phase would not be changed by water infiltration. The wetting and drying process majorly impacts the clay aggregates. The SEM measurement was conducted on the clay aggregates in the specimens of WGS to explore the microscopic mechanism of climatic influence on pore characteristics of the soil. The microscopic morphology of WGS under 0, 1, 3, and 5 wetting-drying cycles is observed through SEM images. As suggested in Fig. 12 (a), clay particles in soil are packed as sheet structures of Kaolin aggregates, contributing to the improvement of soil compactness. The morphological feature of Kaolin aggregates with irregular appearance is mainly arranged in the form of surface-to-surface contact. Besides, few pores with large sizes exist among soil grains. Fig. 12 (b) demonstrates that the presence of microscopic damage results in the increasing number and volume of pores in the tested specimen after the first cycle. In Fig. 12 (c), the small-sized pores among the clay aggregates converse to large pores, and the surface-edge contact begins to appear after three cycles. As illustrated in Fig. 12 (d), the soil microstructure is severely damaged after the specimen experienced five cycles. Additionally, the local cementation material with flat sheets

hydrolyzes and decomposes due to cyclic wetting and drying. Hence, the propagation of pores in WGS mentioned above is also reflected in the observation of the evolutionary characteristics of microstructures.

The near-surface WGS is frequently encountered in an unsaturated or dry state in nature. Subsequently, the mechanical and physical properties would alter due to the reduction of suction forces by wetting when the soil is saturated or its moisture content rapidly increased (Lu et al. 2014, Rahardjo et al. 2004). From the microscopic perspective, the drying and wetting process contributes to pore expansion in WGS. During the wetting process, the swelling force existing in the sidewall of pores is far greater compared to the cohesion in clay aggregates, leading to changes in the mutual effect among mineral particles. During the drying process, the water migration causes uneven shrinkage deformation in clay aggregates, resulting in the expansion of the capillary pores (Burton et al. 2015). Concludingly, the alteration of dry and wet seasons severely reforms the soil microstructure, affecting the pore structure, making the micro-pores gradually expand to form micro-pores, and thus deteriorating the hydraulic properties of WGS.

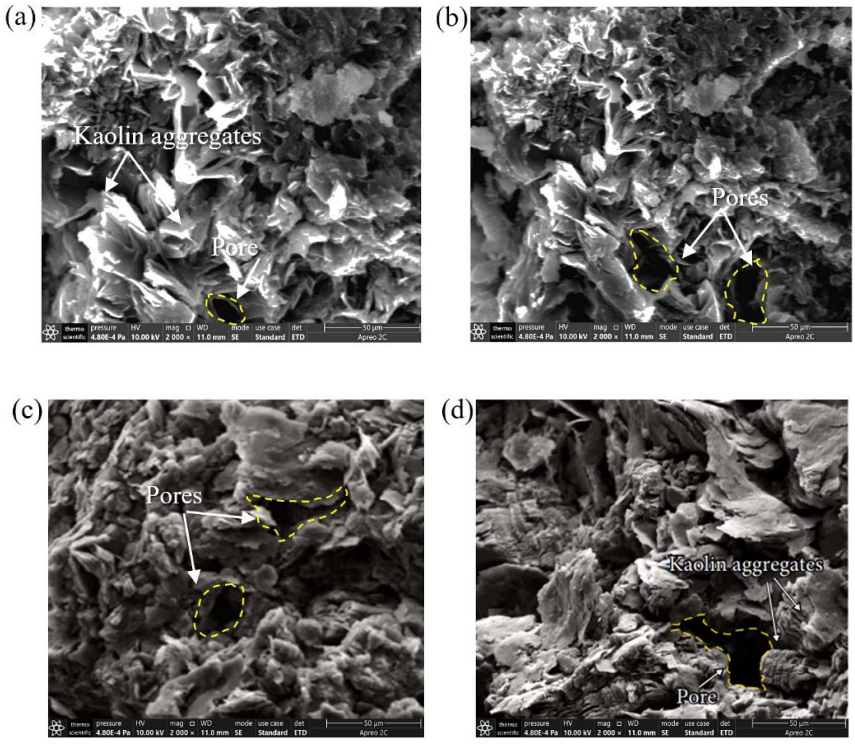


**Fig. 12** SEM images of WGS under different number of wetting-drying cycles: (a) $N$=0; (b) $N$=1; (c) $N$=3; (d) $N$=5.

## 7. Conclusions

In this paper, the effects of multiple wetting-drying cycles on pore distributions of near-surface WGS were investigated using NMR and MIP techniques to reveal the influence of alterations in dry and wet seasons on soil microstructure and the applicability of these two experiments. Upon measurements, the following conclusions were drawn.

(1) From MIP measurements, the cyclic wetting-drying significantly changed the pore size distributions of near-surface WGS by increasing the volume of pores with a diameter smaller than 10 μm while lowering the volume of pores with a diameter smaller than 5 μm.

(2) The $T_2$ spectrums from NMR measurements were characterized by a bimodal distribution. The total area of peaks of WGS was positively related to the accumulative intrusion during the multiple wetting and drying cycles, suggesting the feasibility and accuracy of using NMR data to estimate the soil porosities.

(3) The distributed probability of pore volume with different sizes was calculated from $T_2$ spectrums. After 8 wetting and drying cycles, the proportion of micro-pores decreased from 91.15% to 56.04%, and that of macro-pores increased from 9.85% to 43.96%. Besides, the expansion of pore volumes and the deteriorated degree of soil microstructure were visually observed through the NMR imaging. The significant change in probability distributions of pore volumes and $T_2$-weighted images unveiled that the original pores with small sizes in WGS gradually expanded and connected into large pores or even cracks under the influence of dry and wet seasons.

(4) Comparison and analysis conducted between NMR-based and MIP-based PSDs demonstrated a noticeable difference in the micro-pores of WGS. The NMR measurements with the advantage of testing principle and nondestructive scanning obtained more accurate information on pore distribution.

(5) As implied in the microscopic morphology of WGS, the alteration of dry and wet seasons severely reformed the soil microstructure, affecting the pore structure, making the micro-pores gradually expand to form macro-pores, and thus deteriorating the microstructure of near-surface WGS.

**Declaration of Competing Interest**

The authors declare that they have no known competing financial interests or personal relationships that could have appeared to influence the work reported in this paper.

**Acknowledgments**

The present study had the financial support of the National Natural Science Foundation of China (Grant Nos. 12102312 and 42177148). The aurthors are grateful for the help form anonymous

editors and reviewers.

**Reference**


An, R., Kong, L. W., Zhang, X. W., and Li, C. S. (2022), Effects of dry-wet cycles on three-dimensional pore structure and permeability characteristics of granite residual soil using X-ray micro computed tomography. *Journal of Rock Mechanics and Geotechnical Engineering*, 14(3), 851-860. doi:10.1016/j.jrmge.2021.10.004

An, R., Wang, Y., Zhang, X. W., Chen, C., Liu, X. Y., and Cai, S. T. (2023), Quantitative characterization of drying-induced cracks and permeability of granite residual soil using micron-sized X-ray computed tomography, *Science of the Total Environment*, doi:10.1016/j.scitotenv.2023.163213

An, R., Zhang, X.W., Wang, Y. X., Chen, C., and Gong, J. W. (2022), Freeze-thaw Impact on Sandy Clay in Artificial frozen-walls: an Investigation of Shear Strength and Pore-size Distribution. *International Journal of Geomechanics*, 22(12). doi: 10.1061/(ASCE)GM.1943-5622.0002489

Baer, J. U., Kent, T. F., and Anderson, S. H. (2009), Image analysis and fractal geometry to characterize soil desiccation cracks. *Geoderma*, 154(1-2), 153-163. doi: 10.1016/j.geoderma.2009.10.008

Blight, G. E., and Leong, E. C. (2012), *Mechanics of residual soils*. London: CRC Press.

Burton, G. J., Pineda, J. A., Sheng, D., and Airey, D. (2015), Microstructural changes of an undisturbed, reconstituted and compacted high plasticity clay subjected to wetting and drying. *Eng Geol*, 193, 363–373. doi: 10.1016/j.enggeo.2015.05.010

Burton, G. J., Sheng, D. and Campbell, C. (2014), Bimodal pore sizedistribution of a high-plasticity compacted clay. *Géotechnique Lett. 4*, No. 2, 88–93. doi: 10.1680/geolett.14.00003

Coutinho, R. Q., Silva, M. M., Santos, A. N., and Lacerda, W. A. (2019), Geotechnical characterization and failure mechanism of landslide in granite residual soil. *Journal of Geotechnical and Geoenvironmental Engineering*, 145(8), 05019004. doi:10.1061/(ASCE)GT.1943-5606.0002052

Duan, X. Q., Deng, Y. S., Tao, Y., He, Y. B., Lin, L. R., and Chen, J. Z. (2018), Variation in soil saturated hydraulic conductivity along the hillslope of collapsing granite gullies. *Hydrol. Sci. J.*, 63 (5), 803-817. doi: 10.1080/02626667.2018.1453610.

Fonseca, A. V. D., Fernandes, M. M., and Cardoso, A. S. (1997), Interpretation of a footing load test on a saprolitic soil from granite. *Géotechnique*, 47(3), 633-651. doi: 10.1680/geot.1997.47.3.633

He, Y., Cui, Y. J., Ye, W. M., and Conil, N. (2018), Effects of wetting-drying cycles on the air permeability of compacted Téguline clay. *Eng Geol*, 228, 173-179. doi:10.1016/j.enggeo.2017.08.015

Huang, Z., Zhang, H., Liu, B., Wei, B. X., and Wang, H. (2021), Using CT to test the damage characteristics of the internal structure of expansive soil induced by dry–wet cycles. *AIP Adv*, 11(7), 075305. doi:10.1063/5.0057450

Kenyon, W. E. (1992), Nuclear magnetic resonance as a petrophysical measurement. International Journal of Radiation Applications & Instrumentation.part E. *Nuclear Geophysics*, 6(2), 153-171. doi:10.1016/0892-6875(92)90067-J

Kong, L., Sayem, H. M., and Tian, H. (2018), Influence of drying–wetting cycles on soil-water characteristic curve of undisturbed granite residual soils and microstructure mechanism by nuclear magneticresonance (NMR) spin-spin relaxation time (T2) relaxometry. *Canadian Geotechnical Journal*, 55(2), 208–216. doi:10.1139/cgi-2016-0614

Kusuma, M. D., and Leong, E. C. (2014), Estimating Side Resistance of Bored Pile in Residual Soils. *GEOTECH ENG*, 45(3), 90-95.

Liu, P., Chen, R. P., Wu, K., and Kang, X. (2020), Effects of drying-wetting cycles on the mechanical behavior of reconstituted granite-residual soils. *J Mater Civ Eng*, 32(8), 04020199. doi:10.1061/(ASCE)MT.1943-5533.0003272

Liu, X. Y., Zhang, X. W., Kong, L. W., Wang, G., and Lu, J. F. (2022), Disintegration of granite residual soils with varying degrees of weathering, *Engineering Geology*, 305, 10673. doi:10.1016/j.enggeo.2022.106723

Liu, X., Zhang, X., Kong, L., Wang, G., and Liu, H. (2022), Formation mechanism of collapsing gully in southern China and the relationship with granite residual soil: a geotechnical perspective. *CATENA*, 210, 105890. doi: 10.1016/j.catena.2021.105890

Lu, N., Kaya, M., and Godt, J. W. (2014), Interrelations among the soil-water retention, hydraulic conductivity, and matric potential-stress characteristic curves. *Journal of Geotechnical and Geoenvironmental Engineering*, 140(5), 04014007. doi:10.1061/(ASCE) GT.1943-5606.0001085

Luan, S., Wang, F. L., Wang, T. H., Lu, Z., and Shui, W. H. (2018), Characteristics of Gravelly Granite Residual Soil in Bored Pile Design: An In Situ Test in Shenzhen. *ADV MATER SCI ENG*, 2018, 1-13. doi:10.1155/2018/7598154

456 Meng, F. Y., Chen, R. P., Wu, H. N., Xie, S. W., and Liu, Y. (2020), Observed behaviors of a long and
457 deep excavation and collinear underlying tunnels in Shenzhen granite residual soil. *Tunnelling and*
458 *Underground Space Technology*, 103, 103504. doi:10.1016/j.tust.2020.103504
459 Ng, C. W. W., Xu, J., and Yung, S.Y. (2009), Effects of wetting–drying and stress ratio on anisotropic
460 stiffness of an unsaturated soil at very small strains. *Can Geotech J*, 46(9), 1062–1076.
461 doi:10.1139/T09-043
462 Ohkubo, T., Ibaraki, M., Tachi, Y., and Iwadate, Y. (2016), Pore distribution of water-saturated
463 compacted clay using NMR relaxometry and freezing temperature depression: Effects of density and
464 salt concentration. *Applied Clay Science*, 123, 148-155. doi:10.1016/j.clay.2016.01.014
465 Okewale I. A., and Coop, M.R. (2017), A study of the effects of weathering on soils derived from
466 decomposed volcanic rocks. *Eng Geol*, 222, 53–71. doi:10.1016/j.enggeo.2017.03.014
467 Osterman, G., Keating, K., Binley, A., and Slater, L. (2016), A laboratory study to estimate pore
468 geometric parameters of sandstones using complex conductivity and nuclear magnetic resonance for
469 permeability prediction. *Water Resources Research*, 52, 4321–4337. doi:10.1002/2015WR018472
470 Otalvaro, I. F., Neto, M. P. C., and Delage, P. (2015), Relationship between soil structure and water
471 retention properties in a residual compacted soil. *Eng Geol*, 205, 73-80.
472 doi:10.1016/j.enggeo.2016.02.016
473 Pires, L. F., Auler, A. C., Roque, W. L., and Mooney, S. J. (2020), X-ray microtomography analysis of
474 soil pore structure dynamics under wetting and drying cycles. *Geoderma*, 362, 114103.
475 doi:10.1016/j.geoderma.2019.114103
476 Pires, L. F., Cooper, M., Cássaro, F. A. M., Reichardt, K., Bacchi, O. O. S., and Dias, N. M. P. (2008),
477 Micromorphological analysis to characterize structure modifications of soil samples submitted to
478 wetting and drying cycles. *CATENA*, 72(2), 297-304. doi: 10.1016/j.catena.2007.06.003
479 Rahardjo, H., Aung, K. K., Leong, E. C., and Rezaur, R. B. (2004), Characteristics of residual soils in
480 Singapore as formed by weathering. *Eng Geol*, 73(1–2), 157–169. doi:10.1016/j.enggeo.2004.01.002
481 Rao, S.M., and Revanasiddappa, K. (2006), Influence of cyclic wetting drying on collapse be-haviour
482 of compacted residual soil. *Geotech. Geol. Eng*, 24, 725–734. doi:10.1007/s10706-004-5077-4
483 Robin, V., Paul, S., Arnaud, M., Olivier, R., and Michael, D. (2016), Effective porosity measurements
484 of poorly consolidated materials using non-destructive methods. *Eng Geol*, 205, 24-29.
485 doi:10.1016/j.enggeo.2016.02.007

Starnoni, M., Pokrajac, D., and Neilson, J. E. (2017), Computation of fluid flow and pore-space properties estimation on micro-CT images of rock samples. *Computers & Geosciences*, 106, 118-129. doi:10.1016/j.cageo.2017.06.009

Stingaciu, L. R., Pohlmeier, A., Blumler, P., Weihermuller, L., Van Dusschoten, D., Stapf, S., and Vereecken, H. (2009), Characterization of unsaturated porous media by high-field and low-field NMR relaxometry. *Water Resources Research*, 45, W08412. doi: 10.1029/2008WR007459

Suits, L D., Sheahan, T. C., Leong, E. C., He, L., and Rahardjo, H. (2002), Factors affecting the filter paper method for total and matric suction measurements. *Geotech Test J*, 25(3), 322-333. doi: 10.1520/GTJ11094J

Suzuki, E. (2002), High-resolution scanning electron microscopy of immunogold-labelled cells by the use of thin plasma coating of osmium. *J Microsc*, 208(3), 153-157. doi:10.1046/j.1365-2818.2002.01082.x

Tang, C. S., Cheng, Q., Leng, T., Shi, B., Zeng, H., & Inyang, H. I. (2020). Effects of wetting-drying cycles and desiccation cracks on mechanical behavior of an unsaturated soil. *Catena*, 194, 104721. doi: 10.1016/j.catena.2020.104721

Tian, H. H., and Wei, C. F. (2020), Characterization and quantification ofpore water in clays during drying process with low-field NMR. *Water Resources Research*, 56, e2020WR027537. doi:10.1029/2020WR027537

Tian, H. H., Wei, C. F., and Tan, L. (2019), Effect of freezing-thawing cycles on the microstructure of soils: A two-dimensional NMR relaxation analysis. *Cold Regions Science and Technology*, 158, 106-116. doi:10.1016/j.coldregions.2018.11.014

Tuller, M., and Or, D. (2001), Hydraulic conductivity of variably saturated porous media: Film and corner flow in angular pore space. *Water Resources Research*, 37(5), 1257–1276. doi:10.1029/2000WR900328

Vogel, H. J., Hoffmann, H., Leopold, A., and Roth, K. (2005), Studies of crack dynamics in clay soil. ii. a physically based model for crack formation. *Geoderma*, 125(3-4), 213-223. doi: 10.1016/j.geoderma.2004.07.008

Wang, C., Li, S., Lai, Y., Chen, Q., He, X., Zhang, H., and Liu, X. (2022), Predicting the Soil Freezing Characteristic From the Particle Size Distribution Based on Micro-Pore Space Geometry. *Water Resources Research*, 58, e2021WR030782. doi:10.1029/2021WR030782

Washburn, E. W. (1921), The dynamics of capillary flow. *Phys.rev.ser*, 17(3), 273-283. doi:10.1103/PhysRev.17.273

Watanabe, K., and Osada, Y. (2016), Comparison of hydraulic conductivity in frozen saturated and unfrozen unsaturated soils. *Vadose Zone Journal*, 15(5), 1-7. doi:10.2136/vzj2015.11.0154

Webber, J. B., Corbett, P., Semple, K. T., Ogbonnaya, U., and Teel, W. S. (2013), An NMR study of porous rock and biochar containing organic material. *Microporous and Mesoporous Materials*, 178, 94-98. doi:10.1016/j.micromeso.2013.04.004

Yao, Y. B., and Liu, D. M. (2012), Comparison of low-field NMR and mercury intrusion porosimetry in characterizing pore size distributions of coals. *Fuel*, 95, 152-158. doi: 10.1016/j.fuel.2011.12.039

Ying, Z., Cui, Y. J., Benahmed, N., and Duc, M. (2021), Drying effect on the microstructure of compacted salted silt. *Géotechnique*, 1-34, doi: 10.1680/jgeot.20.P.319

Yu, H. H., Sunb, D., and Tian, H. H. (2019), NMR-based analysis of shear strength of weakly expansive clay in sodiumchloride solution. *Magnetic Resonance Imaging*, 58, 6–13. doi:10.1016/j.mri.2019.01.002

Zhang, X. W., Liu, X. Y., Chen, C., Xu, Y. Q., and Liu, H. H. (2022), Evolution of disintegration properties of granite residual soil with microstructure alteration due to wetting and drying cycles. *Bulletin of Engineering Geology and the Environment*, 81(3), 93. doi:10.1007/s10064-022-02602-5

Zhang, X. W., Kong, L. W., Yin, S., and Chen, C. (2017), Engineering geology of basaltic residual soil in Leiqiong, southern China. *Eng. Geol*, 220, 196–207. doi: 10.1016/j.enggeo.2017.02.002

Zhang, X. W., Liu, X. Y., Xu, Y. Q., Wang, G., and Ren, Y. B. (2023), Compressibility, permeability and microstructure of fine-grained soils containing diatom microfossils. *Géotechnique*, 1-15. doi: 10.1680/jgeot.22.00155

Zhao, N. F., Ye, W. M., Chen, Y. G., Chen, B., and Cui, Y. J. (2019), Investigation on swelling-shrinkage behavior of unsaturated compacted GMZ bentonite on wetting-drying cycles. *Bull Eng Geol Environ*, 78, 617-627. doi: 10.1007/s10064-017-1095-3

**Figure 1.**

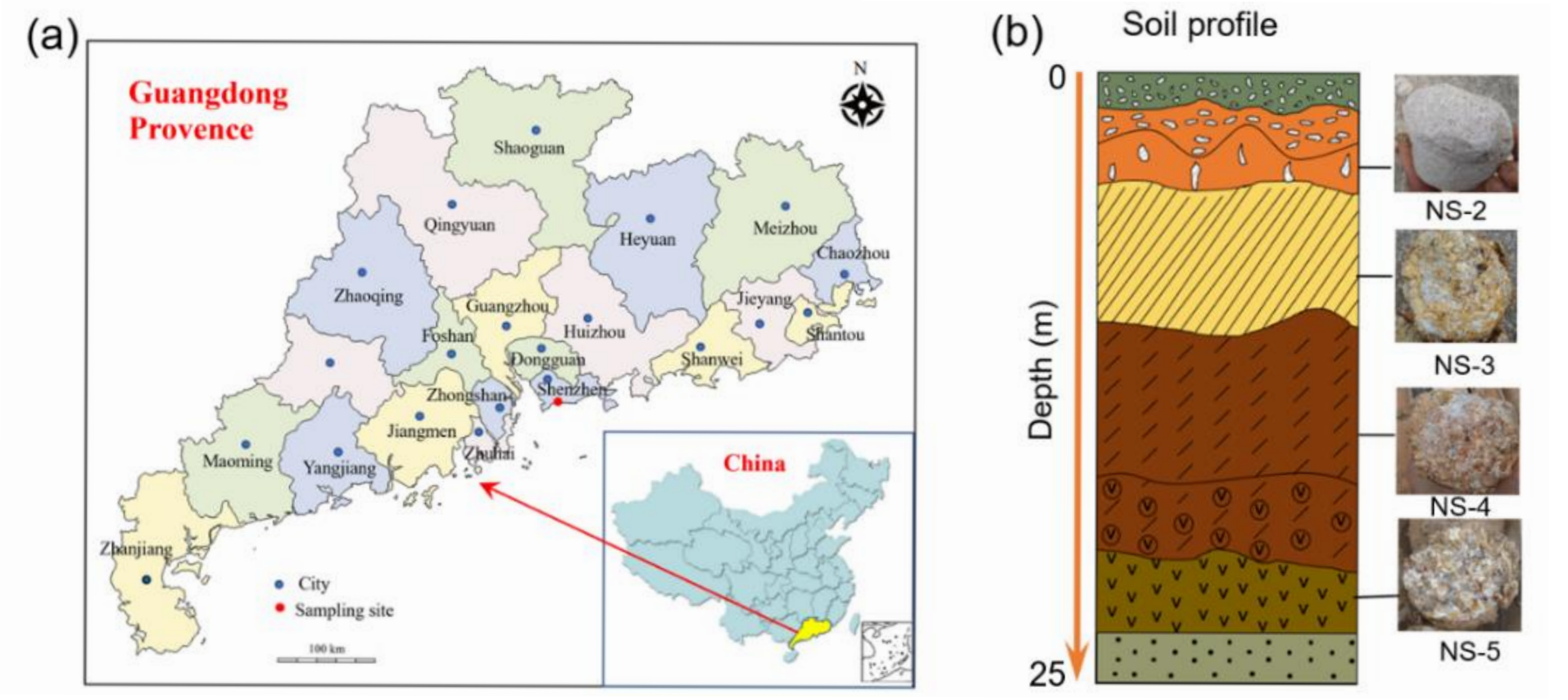
(a)
Guangdong Provence
N
Shaoguan
Qingyuan
Heyuan
Meizhou
Chaozhou
Zhaoqing
Guangzhou
Jieyang
Foshan
Huizhou
Shantou
Dongguan
Shanwei
Shenzhen
Zhongshan
Jiangmen
Zhuhai
Maoming
Yangjiang
Zhanjiang
City
Sampling site
100 km
China
(b)
Soil profile
0
Depth (m)
25
NS-2
NS-3
NS-4
NS-5

**Figure 2.**

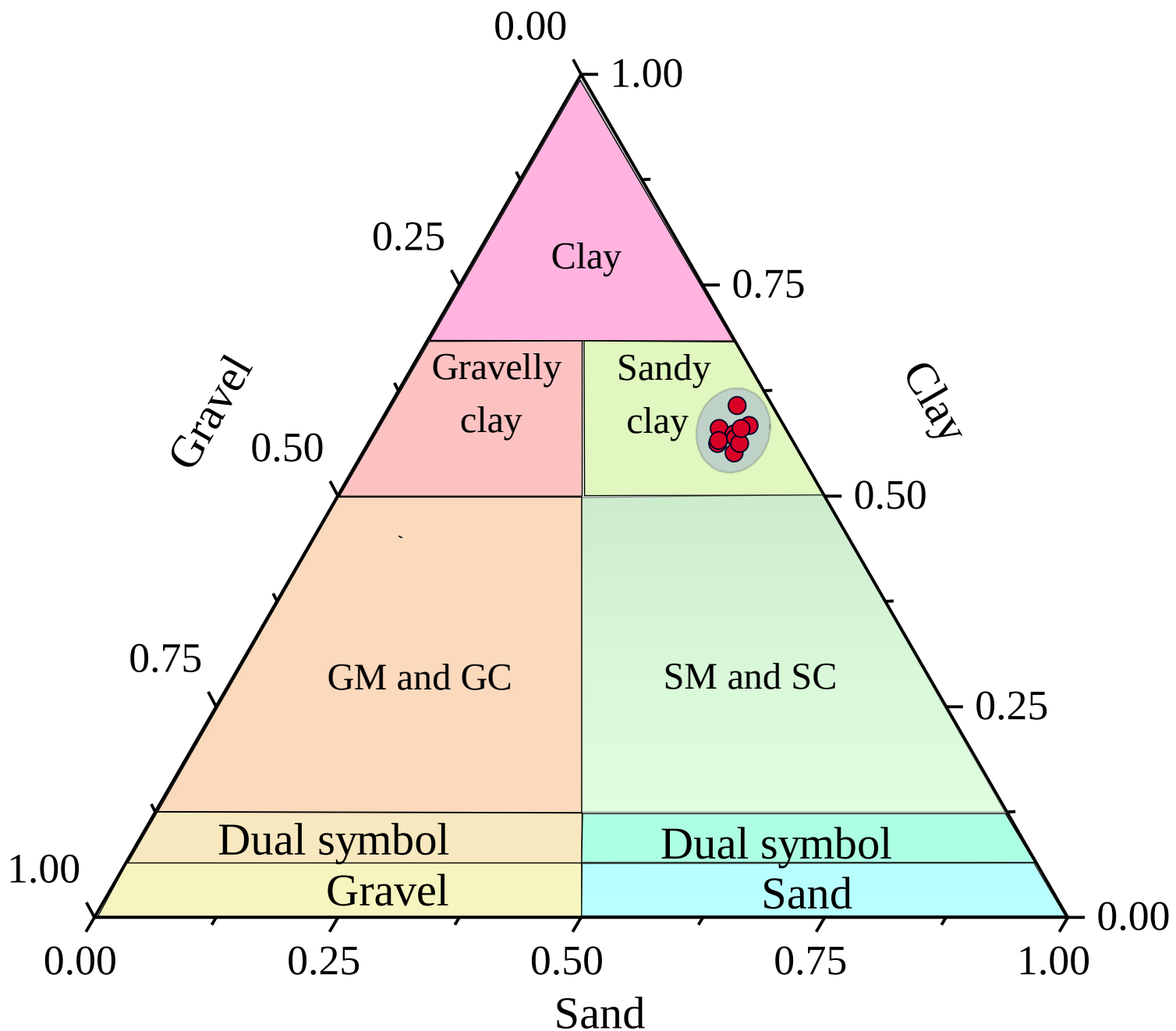
0.00
1.00
0.25
0.75
0.50
0.50
0.75
0.25
1.00
0.00
Gravel
Clay
Clay
Gravelly clay
Sandy clay
GM and GC
SM and SC
Dual symbol
Gravel
Dual symbol
Sand
0.00
0.25
0.50
0.75
1.00
Sand

**Figure 3.**

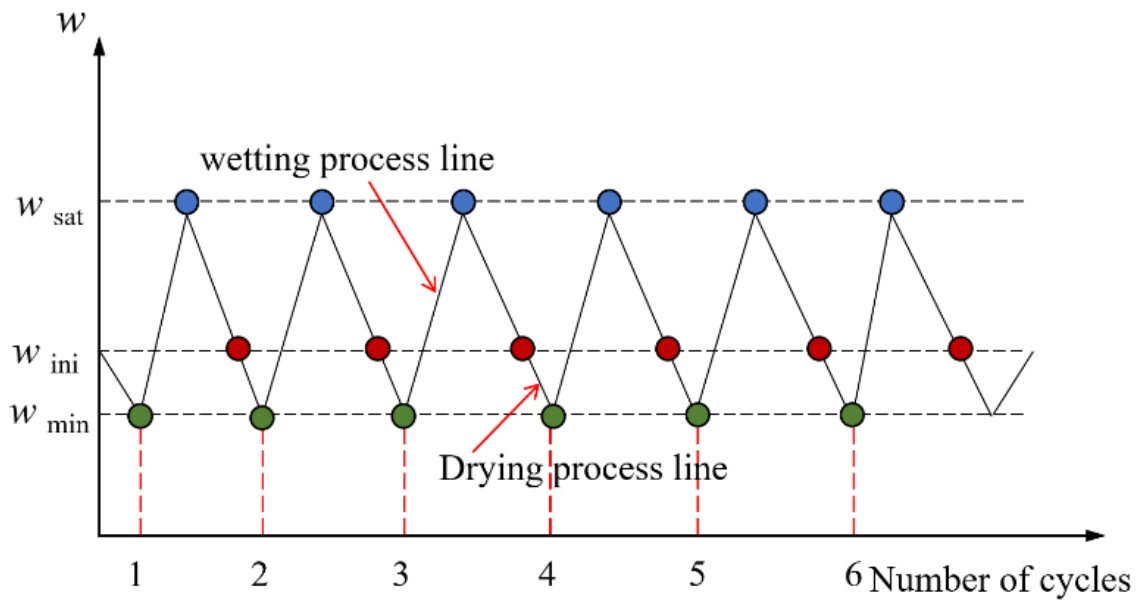
w
wetting process line
w sat
w ini
w min
Drying process line
1
2
3
4
5
6
Number of cycles

**Figure 4.**

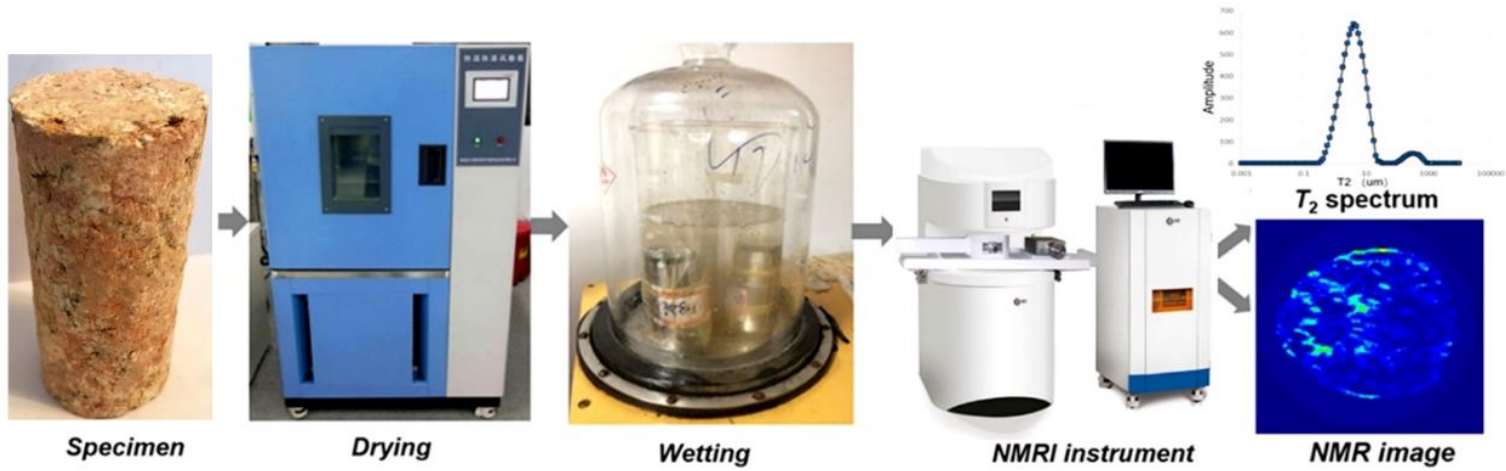
Amplitude
T2 (um)
$T_2$ spectrum
Specimen
Drying
Wetting
NMRI instrument
NMR image

**Figure 5.**

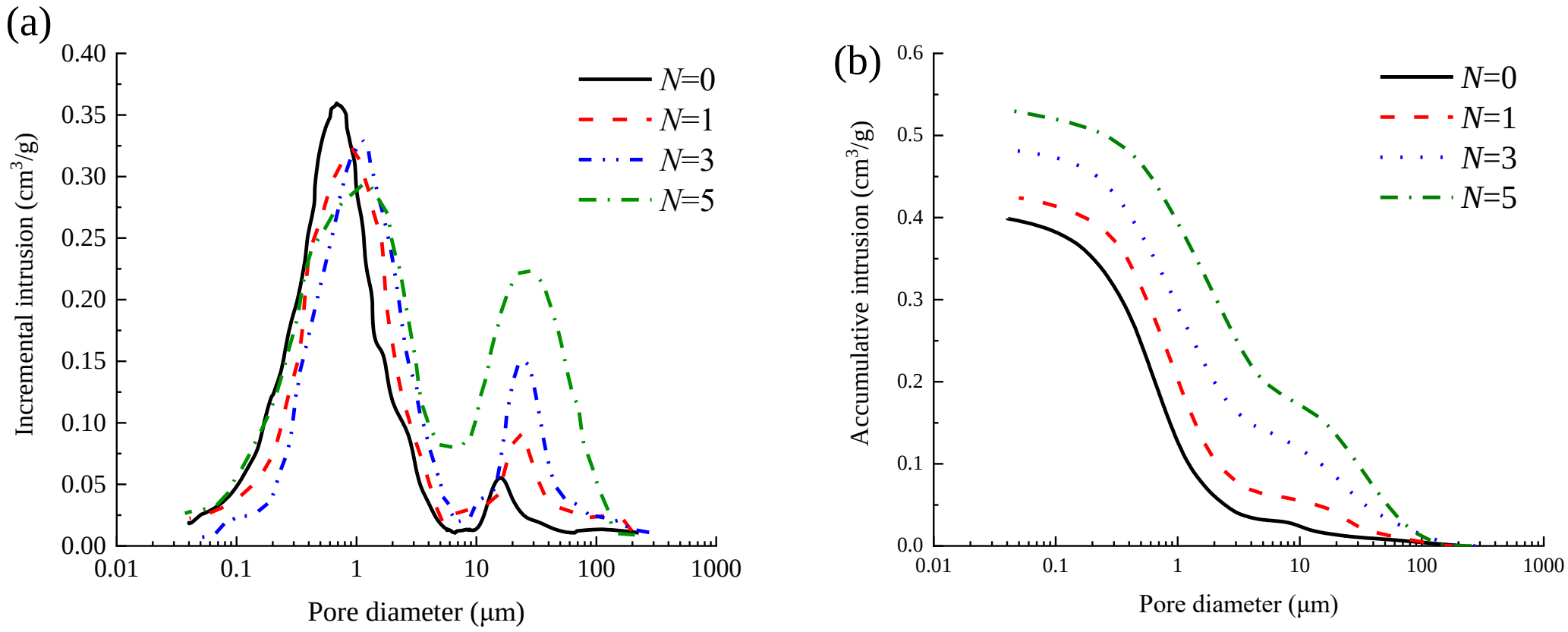
(a)
Incremental intrusion (cm3/g)
0.40
0.35
0.30
0.25
0.20
0.15
0.10
0.05
0.00
0.01
0.1
1
10
100
1000
Pore diameter (μm)
N=0
N=1
N=3
N=5
(b)
Accumulative intrusion (cm3/g)
0.6
0.5
0.4
0.3
0.2
0.1
0.0
0.01
0.1
1
10
100
1000
Pore diameter (μm)
N=0
N=1
N=3
N=5

**Figure 6.**

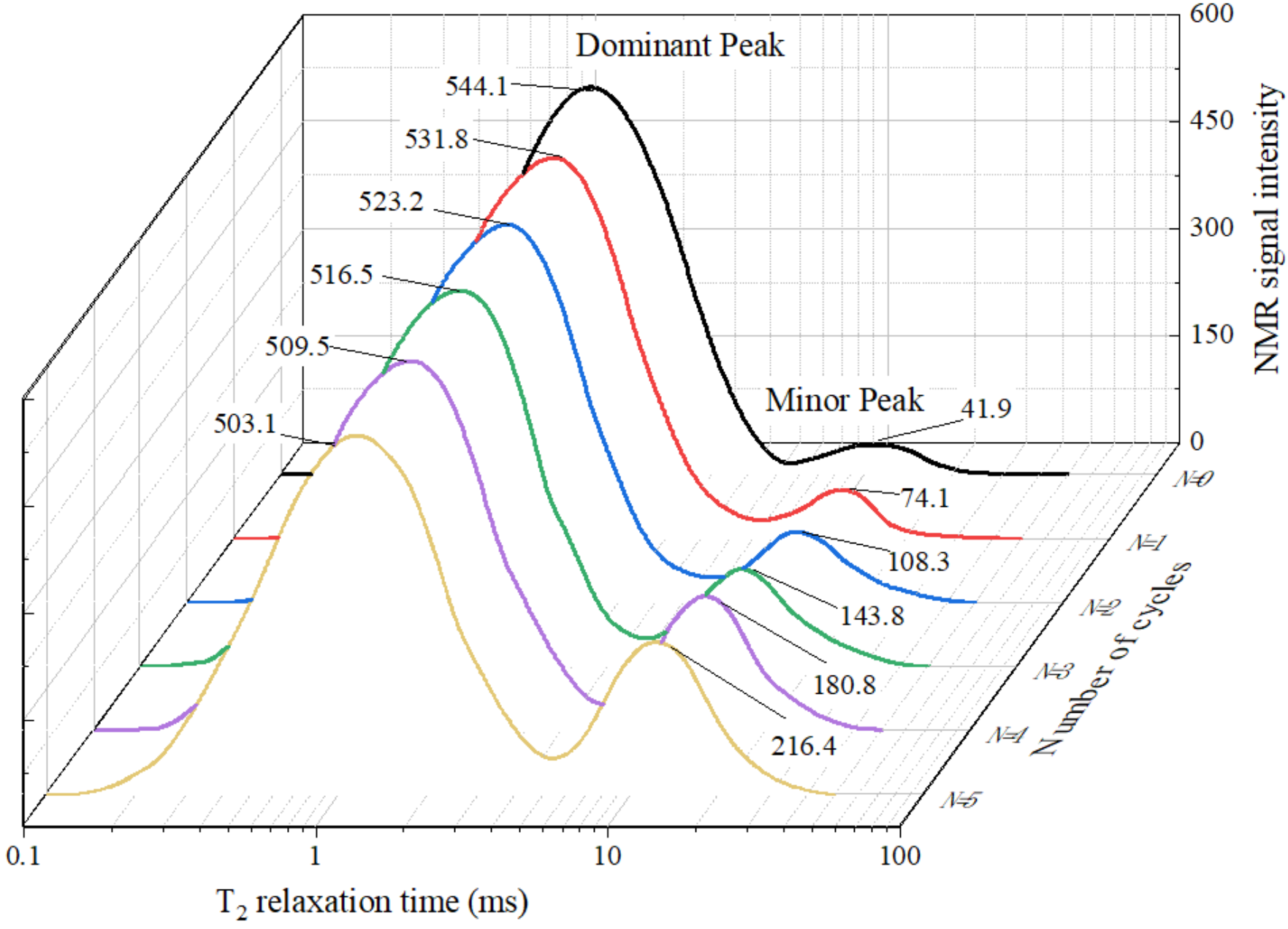
Dominant Peak
544.1
531.8
523.2
516.5
509.5
503.1
Minor Peak
41.9
74.1
108.3
143.8
180.8
216.4
600
450
300
150
0
NMR signal intensity
N=0
N=1
N=2
N=3
N=4
N=5
Number of cycles
0.1
1
10
100
T2 relaxation time (ms)

**Figure 7.**

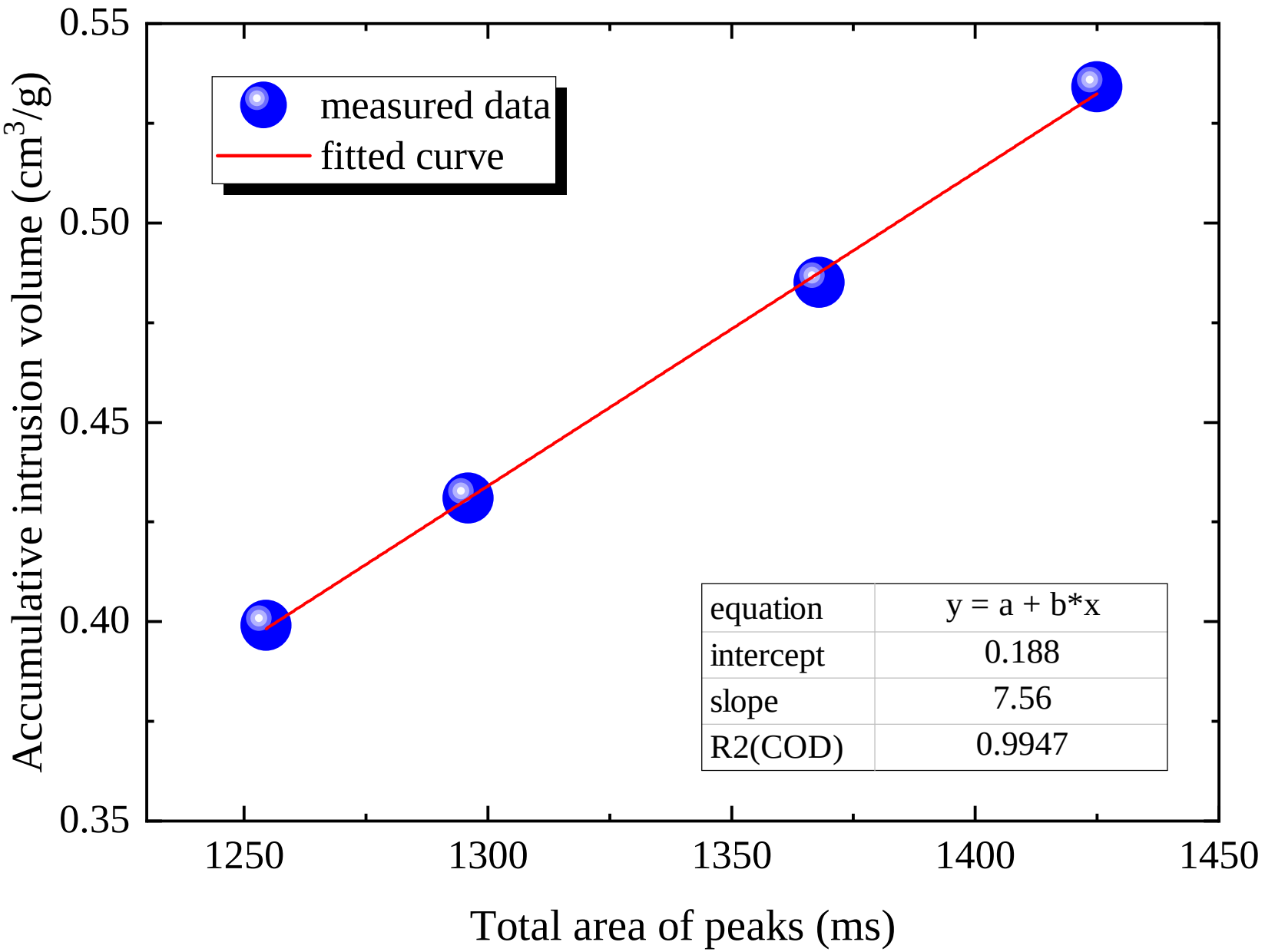
measured data
fitted curve
Accumulative intrusion volume (cm3/g)
0.55
0.50
0.45
0.40
0.35
1250
1300
1350
1400
1450
Total area of peaks (ms)
equation
y = a + b*x
intercept
0.188
slope
7.56
R2(COD)
0.9947

**Figure 8.**

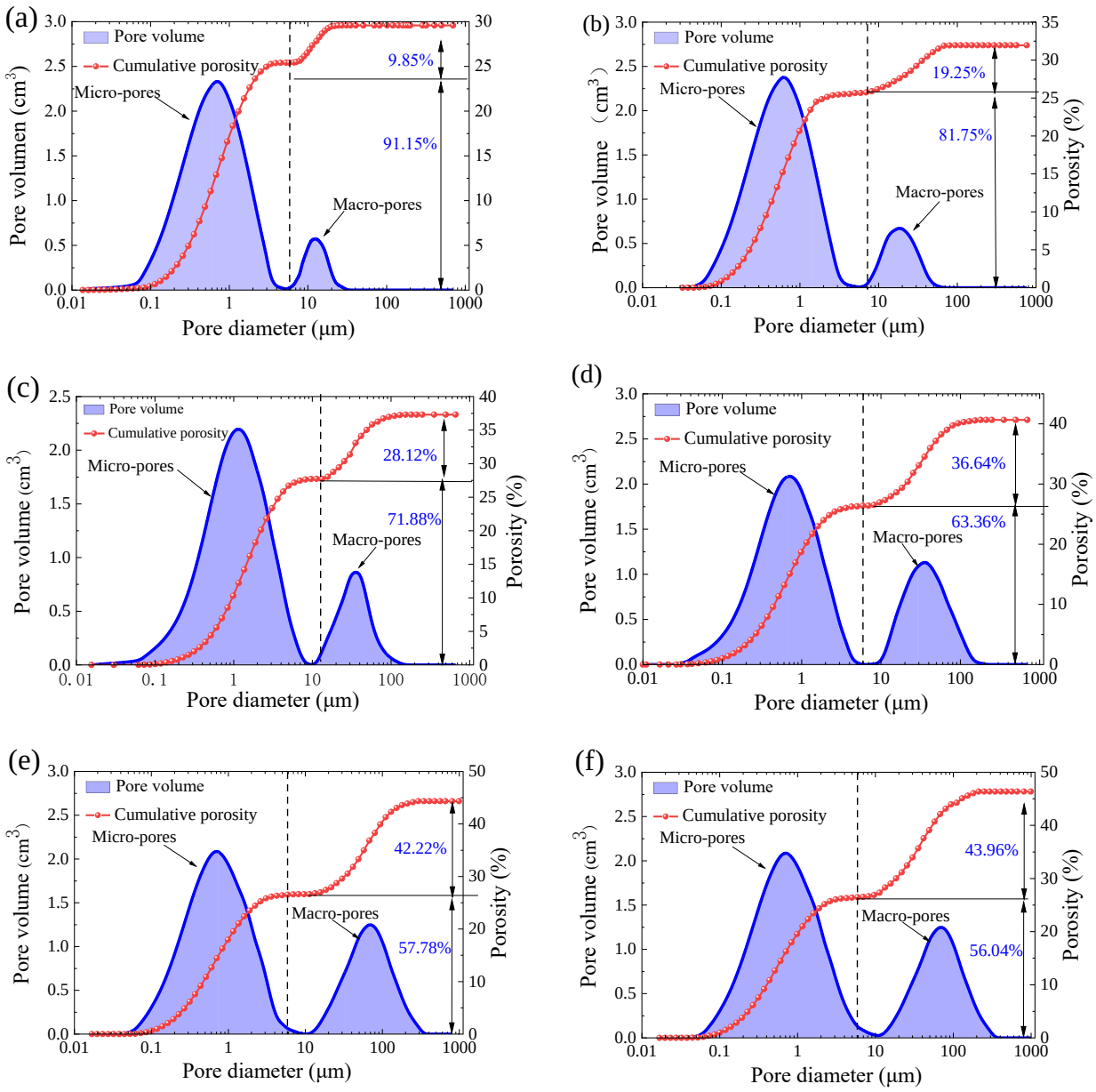
(a)
Pore volume
Cumulative porosity
Micro-pores
Macro-pores
9.85%
91.15%
Pore volumen (cm3)
Porosity (%)
Pore diameter (μm)
(b)
Pore volume
Cumulative porosity
Micro-pores
Macro-pores
19.25%
81.75%
Pore volume (cm3)
Porosity (%)
Pore diameter (μm)
(c)
Pore volume
Cumulative porosity
Micro-pores
Macro-pores
28.12%
71.88%
Pore volume (cm3)
Porosity (%)
Pore diameter (μm)
(d)
Pore volume
Cumulative porosity
Micro-pores
Macro-pores
36.64%
63.36%
Pore volume (cm3)
Porosity (%)
Pore diameter (μm)
(e)
Pore volume
Cumulative porosity
Micro-pores
Macro-pores
42.22%
57.78%
Pore volume (cm3)
Porosity (%)
Pore diameter (μm)
(f)
Pore volume
Cumulative porosity
Micro-pores
Macro-pores
43.96%
56.04%
Pore volume (cm3)
Porosity (%)
Pore diameter (μm)

**Figure 9.**

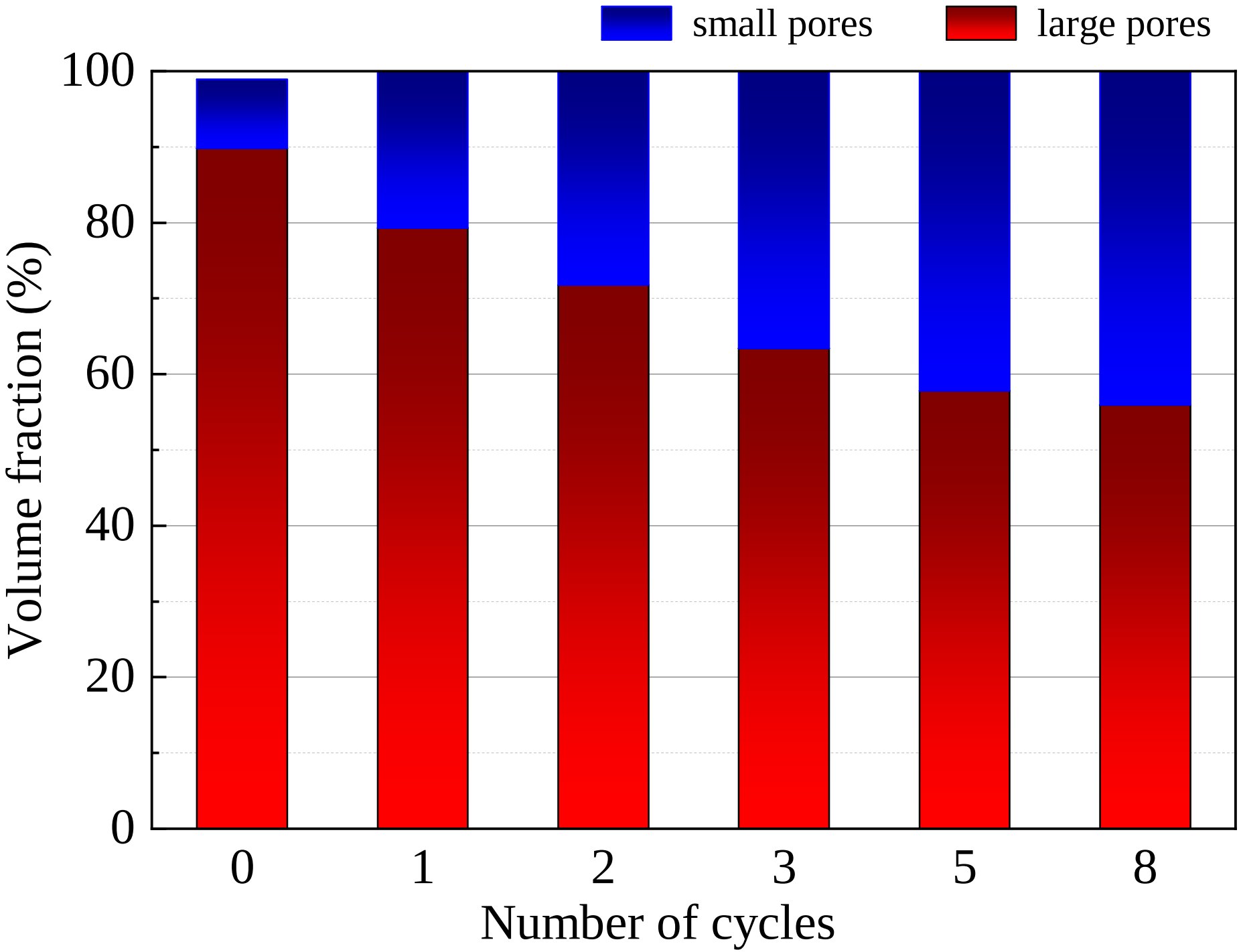
small pores
large pores
100
80
60
40
20
0
Volume fraction (%)
0
1
2
3
5
8
Number of cycles

**Figure 10.**

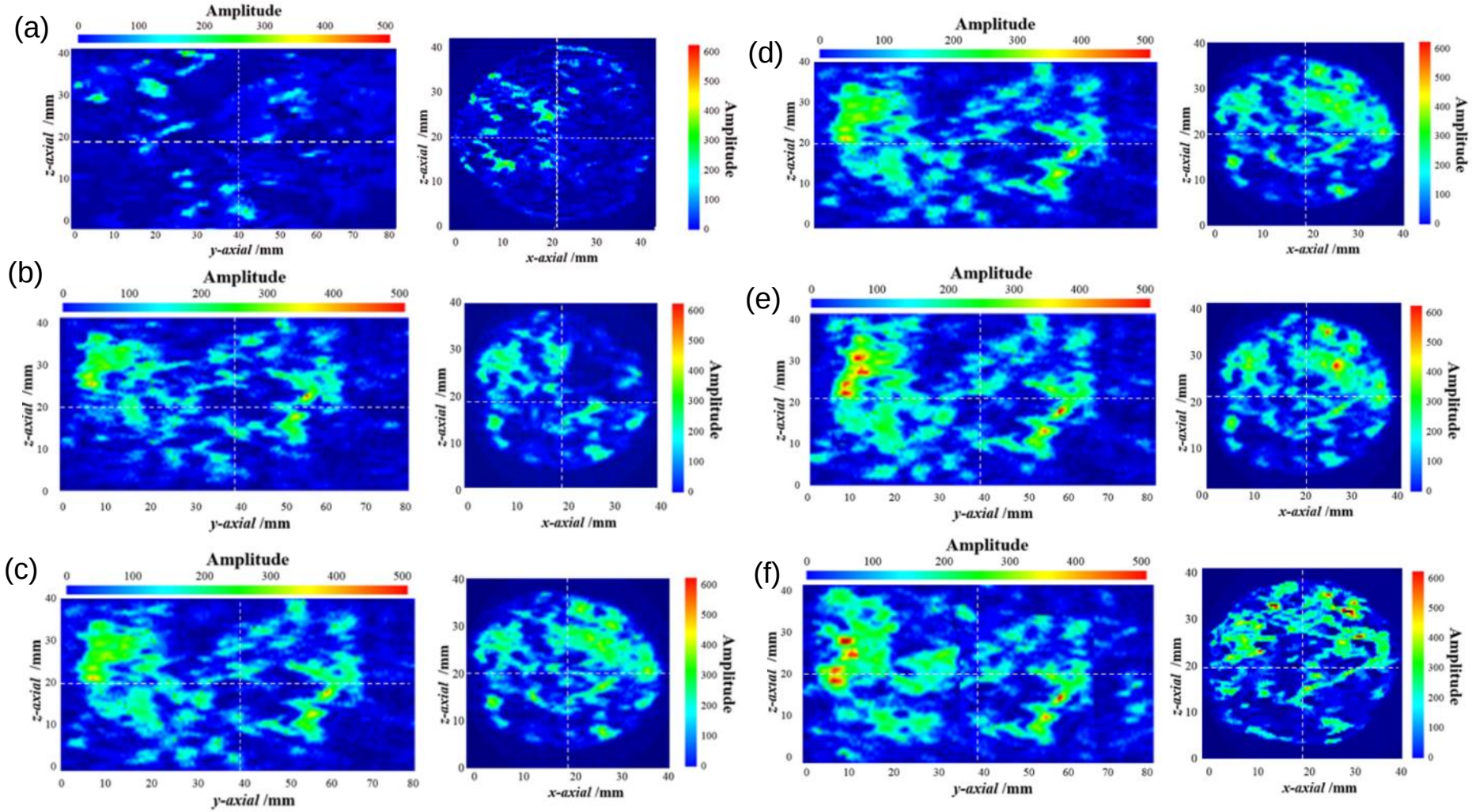
(a)
(b)
(c)
(d)
(e)
(f)
Amplitude
0 100 200 300 400 500
z-axial /mm
y-axial /mm
x-axial /mm
0 10 20 30 40 50 60 70 80
0 10 20 30 40
600 500 400 300 200 100 0
Amplitude

**Figure 11.**

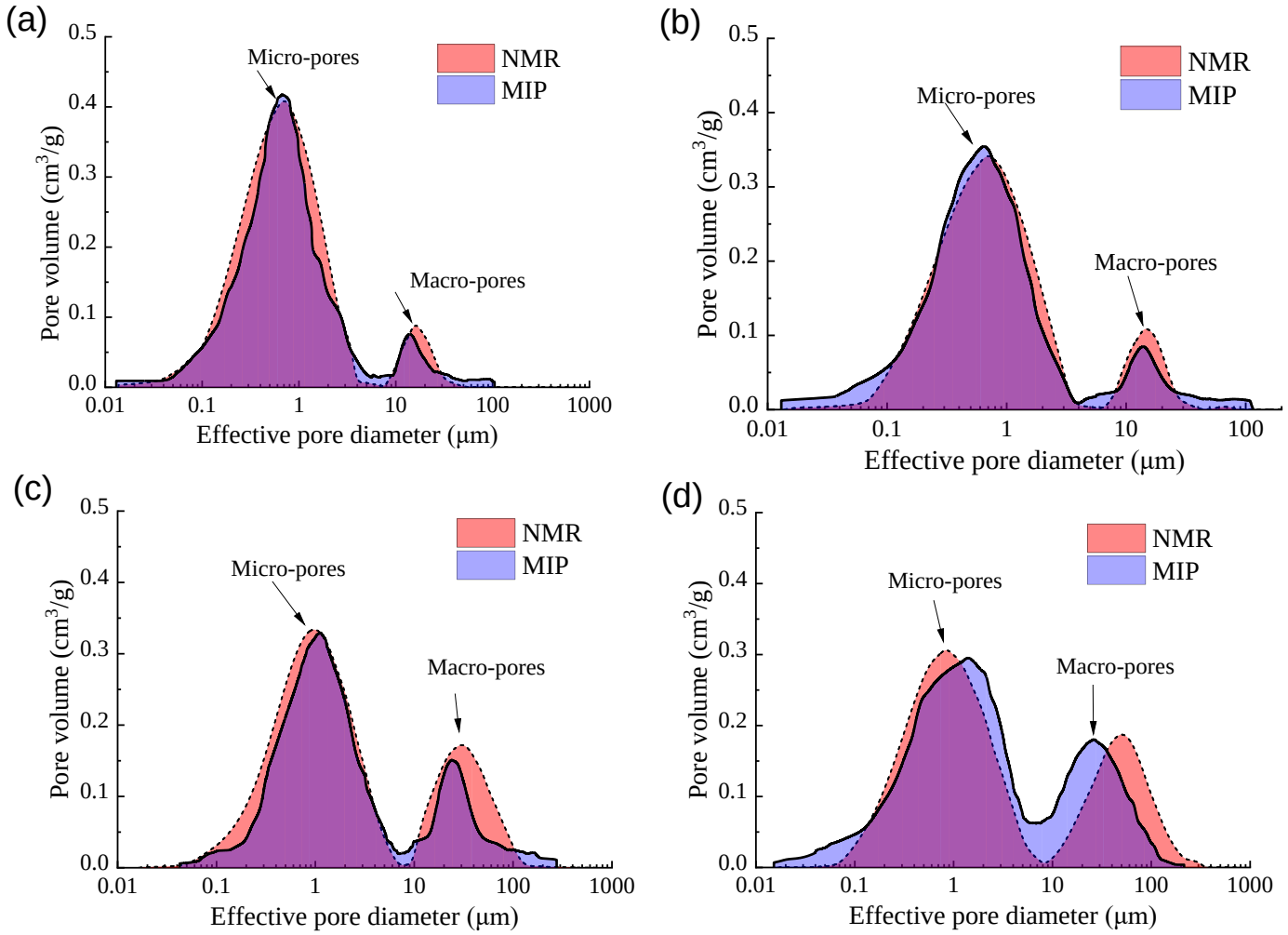
(a)
Micro-pores
Macro-pores
NMR
MIP
Pore volume (cm3/g)
Effective pore diameter (μm)
0.0
0.1
0.2
0.3
0.4
0.5
0.01
0.1
1
10
100
1000
(b)
Micro-pores
Macro-pores
NMR
MIP
Pore volume (cm3/g)
Effective pore diameter (μm)
(c)
Micro-pores
Macro-pores
NMR
MIP
Pore volume (cm3/g)
Effective pore diameter (μm)
(d)
Micro-pores
Macro-pores
NMR
MIP
Pore volume (cm3/g)
Effective pore diameter (μm)

**Figure 12.**

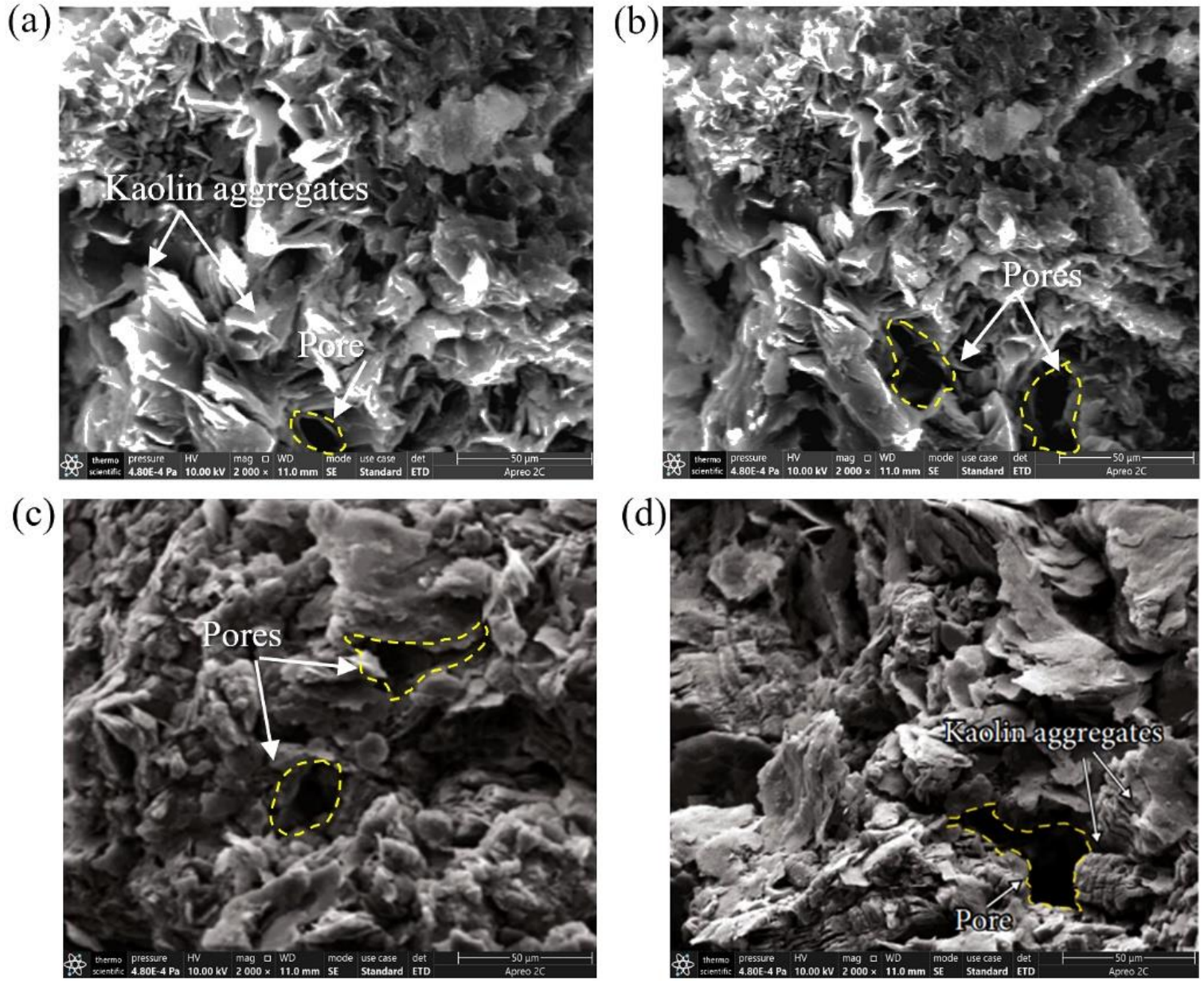
(a)
Kaolin aggregates
Pore
(b)
Pores
(c)
Pores
(d)
Kaolin aggregates
Pore
thermo scientific pressure 4.80E-4 Pa HV 10.00 kV mag 2 000 x WD 11.0 mm mode SE use case Standard det ETD 50 µm Apreo 2C

**Table 1** Physical and mineralogical properties of the WGS.

| Index | Average value |
|---|---|
| Moisture content, $w_n$ (%) | 26.8 |
| Bulk density, $\rho_b$ (g/cm$^3$) | 1.76 |
| Void ratio, $e$ (%) | 0.68 |
| Liquid limit, $w_L$ (%) | 56.4 |
| Plasticity limit, $w_P$ (%) | 24.3 |
| Plasticity index, $I_P$ | 32.1 |
| Hydraulic conductivity, $K$ (cm/s) | $8.5\times10^{-6}$ |
| Unconfined compressive strength (kPa) | 178.6 |
| Effective Cohesion, $c'$ (kPa) | 47.5 |
| Effective internal friction angle, $\varphi'$ (°) | 24.8 |